



HAL
open science

Statistical Narrow Band model for vibrational nonequilibrium CO₂ radiation

Guillaume Janodet, Philippe Rivière, Jean-Michel Lamet, Valérie Rialland,
Lionel Tessé, Anouar Soufiani

► **To cite this version:**

Guillaume Janodet, Philippe Rivière, Jean-Michel Lamet, Valérie Rialland, Lionel Tessé, et al.. Statistical Narrow Band model for vibrational nonequilibrium CO₂ radiation. *Journal of Quantitative Spectroscopy and Radiative Transfer*, 2023, 314, pp.108856. 10.1016/j.jqsrt.2023.108856 . hal-04220093v2

HAL Id: hal-04220093

<https://hal.science/hal-04220093v2>

Submitted on 8 Dec 2023

HAL is a multi-disciplinary open access archive for the deposit and dissemination of scientific research documents, whether they are published or not. The documents may come from teaching and research institutions in France or abroad, or from public or private research centers.

L'archive ouverte pluridisciplinaire **HAL**, est destinée au dépôt et à la diffusion de documents scientifiques de niveau recherche, publiés ou non, émanant des établissements d'enseignement et de recherche français ou étrangers, des laboratoires publics ou privés.

Statistical Narrow Band model for vibrational nonequilibrium CO₂ radiation

Guillaume Janodet^{a,b,c}, Philippe Rivière^{a,*}, Jean-Michel Lamet^b, Valérie Riolland^c, Lionel Tessé^d, Anouar Soufiani^a

^a*Laboratoire EM2C, CNRS, CentraleSupélec, Université Paris Saclay, 3 rue Joliot Curie, 91192 Gif-sur-Yvette Cedex, France*

^b*ONERA/DMPE, Université de Toulouse, F-31055, Toulouse, France*

^c*ONERA/DOA, Université Paris-Saclay, BP80100, 91123 Palaiseau Cedex, France*

^d*ONERA/DMPE, Université Paris-Saclay, F-92322, Châtillon, France*

Abstract

This paper presents the development of a Statistical Narrow Band (SNB) model for CO₂ in a nonequilibrium vibrational state. The population densities of the energy levels are modeled by a three-temperature approach (T, T_{12}, T_3) associated resp. to translation-rotation modes, symmetric-stretching and bending modes, and antisymmetric stretching mode, to compute nonequilibrium line by line (LBL) spectra. The nonequilibrium between vibrational temperatures induces spectral correlation issues between $\eta_\sigma/\kappa_\sigma$ and κ_σ , where η_σ and κ_σ are the emission and absorption coefficients respectively. To overcome this issue, a vibrational splitting of the spectroscopic database is made to separate lines with completely different vibrational transitions. The SNB parameters are obtained by fitting the curves of growth from the LBL approach by a least squares error minimization using a Newton method for pure Lorentz and Doppler broadening regimes for each line class. The total SNB

*Corresponding author.

Email address: philippe.riviere@centralesupelec.fr (Philippe Rivière)

transmissivity is obtained by computing the product of each line class transmissivity, and the decorrelation between the spectra of the different classes is checked. Finally, the model is tested in Voigt broadening regime using a mixing rule by computing outlet radiative intensity of uniform and non-uniform columns and agrees well with the LBL approach. SNB parameters are available under request to the corresponding author.

Keywords: CO₂ radiation, Vibrational nonequilibrium, SNB model

1 **1. Introduction**

2 The Local Thermodynamic Equilibrium (LTE) assumption is no longer valid
3 when internal relaxation time scales become comparable or higher than hydrodynamic time scales in gas flows. The gas is then under the Non-Local
4 Thermodynamic Equilibrium (NLTE) state, which means that it contains an
5 excess or a lack of internal energy compared to translational energy or even a
6 non-Boltzmannian distribution of the populations of the different vibrational
7 levels. This nonequilibrium aspect is found, for instance, in atmospheric entry
8 flows [1, 2], electrically excited or gas dynamic CO₂ lasers [3, 4], or
9 expanding flows like rocket plumes at high altitudes [5]. This departure from
10 LTE affects the radiative properties of the radiating species and thus needs
11 to be considered for radiative transfer.

13

14 One of the challenges in studying the radiation of gases under NLTE conditions is the knowledge of the population of each rovibrational energy level.
15 The detailed vibrational state-to-state approach [6] is a priori the most accurate model for predicting level population densities. However, the total
16
17

18 number of vibrational states of CO₂ with energies lower than the dissociation
19 limit is estimated to be of the order of 10⁵ [7]. Although some models
20 attempt to bin vibrational levels based on physical arguments in order to
21 reduce the computational complexity (see e.g., [7, 8]), the vibrational state-
22 to-state approach remains impracticable in the context of radiative transfer
23 calculations for coupled simulations in complex geometries. Moreover, the
24 uncertainty about the kinetic rate constants of high-energy levels makes using
25 the state-to-state approach very difficult. Therefore, the multi-temperature
26 description of the thermodynamic state of CO₂, based on previous works
27 [9, 10], is adopted in this study to compute vibrational level populations.

28

29 Once the spatial distributions of population densities are known, line-by-line
30 (LBL) local absorption and emission spectra can be computed using suitable
31 spectroscopic databases such as HITRAN [11], HITEMP [12] or CDSD-4000
32 [13] for CO₂ at high temperature. Such LBL calculations have been recently
33 undertaken by Binauld et al. [9] to evaluate the effects of vibrational CO₂
34 NLTE on the infrared radiation emitted by an expanding flow in a conical
35 nozzle or by high-altitude rocket plumes. It was shown in this study that the
36 partial freeze of CO₂ vibration excitation, due to the strong expansion of the
37 flow in the low-pressure atmosphere, may significantly increase the emission
38 by the plume compared to the emission predicted from a single translation
39 temperature. However, the LBL calculations were limited to some chosen
40 lines of sight in the plume and 1D radiation calculations in the case of the
41 nozzle flow. As for the state-to-state kinetic approach, the detailed LBL
42 calculations also remain impracticable when the radiative transfer is to be

43 coupled to flow-field calculations. Indeed, spectral, angular, and spatial in-
44 tegrations would require huge CPU time and storage capabilities. The de-
45 velopment of accurate spectral band models is then highly desirable in this
46 perspective.

47

48 In the framework of radiative transfer spectral modelling in nonequilibrium
49 reentry flows, k-distribution models were first developed by Bansal et al. for
50 N and O atomic radiation [14, 15] and then extended by Bansal et al. [16]
51 to diatomic molecular species (N_2 , N_2^+ , NO, and O_2). Several spectral wide-
52 band binning strategies and reduced order models have been compared in
53 [17] for different reentry conditions. However, in the present work, global
54 and wide-band models are excluded since one of the goals of the present
55 study is to develop models suitable for spectrally integrated radiative trans-
56 fer calculations and also for infrared signature simulations, which are limited
57 to narrow spectral bands.

58

59 Among narrow-band models, k-distribution, with or without an extension
60 with fictitious gases [18], remains challenging to apply in the case of react-
61 ing media with spatial change of chemical composition and strong pressure
62 gradients. Statistical narrow-band models have been applied by Lamet et al.
63 [19] for the prediction of radiative transfer in earth reentry flows and show
64 a good ability to deal with diatomic molecules with the imbalance between
65 electronic/vibration and translation/rotation (two-temperature description
66 of the medium).

67

68 It is worth noticing that all NLTE radiation models mentioned above were
69 dedicated to atomic or diatomic radiation, and none of them has consid-
70 ered polyatomic molecules like CO₂, where a disequilibrium may exist be-
71 tween the different vibration modes. Specific models have been developed
72 for NLTE CO₂ radiation in [20]. However, the smeared band model was
73 employed to get tractable simulations, which may fail for low-pressure ap-
74 plications with well-separated non-optically thin rotational lines. Another
75 approach was developed first by Kudryavtsev and Novikov [21], and then
76 by Vitkin et al. [22, 23], on the basis of statistical narrow-band mixing of
77 lines belonging to different vibrational transitions. However, instead of using
78 accurate spectroscopic databases, semi-analytical simplified models were em-
79 ployed to represent the spectral structure of CO₂ bands in the 4.3 and 2.7 μm
80 regions. This approach was followed by Molchanov et al. [24] who used k -
81 distribution method to compute partial transmissivities in the narrow bands.

82

83 This paper aims to develop a three-temperature SNB model for CO₂, con-
84 sidering spectral correlations and disequilibrium between vibrational modes
85 (Section 2). CO₂ translational and rotational modes are assumed to be at
86 local equilibrium and are described by a single temperature T due to the
87 fast translation-rotation exchanges. Vibrational levels are assumed to fol-
88 low a Boltzmann distribution at a single temperature T_{12} for the symmetric
89 stretching mode and the two-fold degenerate bending mode, due to Fermi
90 Resonance [25] and to fast transfer between polyads with the same antisym-
91 metric stretching mode quantum numbers [26], and a Boltzmann distribution
92 at a different temperature T_3 for the antisymmetric stretching mode. The

93 model is then applied in Section 3 to a simple expanding supersonic nozzle
 94 flow and to radiative transfer along selected lines of sight in the high altitude
 95 plume of a solid propellant rocket as in [9]. The model accuracy is assessed
 96 through comparisons with line-by-line calculations.

97 2. SNB formulation

98 2.1. Radiative properties and multi-temperature model

99 The emission and absorption coefficients for wavenumber σ can be expressed
 100 under the assumption of independent lines as:

$$\eta_\sigma = \sum_{u-l} n_u \frac{A_{ul}}{4\pi} h c \sigma_{ul} f_{ul}(\sigma - \sigma_{ul}), \quad (1)$$

101

$$\kappa_\sigma = \sum_{u-l} (n_l B_{lu} - n_u B_{ul}) h \sigma_{ul} f_{ul}(\sigma - \sigma_{ul}), \quad (2)$$

102 where n_u and n_l are the populations of levels u and l , A_{ul} , B_{ul} and B_{lu}
 103 are the Einstein coefficients for spontaneous emission, induced emission, and
 104 absorption, σ_{ul} is the central wavenumber, and $f_{ul}(\sigma - \sigma_{ul})$ is the spectral
 105 line profile (assumed to be the same for the three radiative mechanisms) of
 106 the transition $u - l$. Spectroscopic data for CO₂ (Einstein coefficients, level
 107 energies, line positions, collisional broadening parameters) have been taken
 108 from the HITEMP-2010 [12] compilation, which has been recommended for
 109 applications up to 2000 K [13]. The population of any rovibrational level k
 110 of CO₂ in the multi-temperature approach of [9] can be expressed as follows:

$$n_k = n_{CO_2} Ab_I \frac{g_k}{Z_I(T, T_{12}, T_3)} \exp\left(-\frac{E^{rot}\{k\}}{k_B T} - \frac{E^{\nu_{12}}\{k\}}{k_B T_{12}} - \frac{E^{\nu_3}\{k\}}{k_B T_3}\right), \quad (3)$$

111 where n_{CO_2} is the total population density of CO₂, Ab_I is the abundance
 112 of the considered isotopologue I , g_k is the degeneracy of the level k . The

113 partitioning scheme of the energy is composed of a rotational part $E^{rot}\{k\}$, a
 114 vibrational part $E^{\nu_{12}}\{k\}$ associated with the coupled symmetric stretching-
 115 bending modes (ν_1, ν_2) and a vibrational part $E^{\nu_3}\{k\}$ corresponding to the
 116 asymmetric stretching mode ν_3 . For each rovibrational level, these energies
 117 are calculated from the spectroscopic database according to

$$E^{rot}\{v_1, \ell_2, v_3, r, \varpi, J\} = E\{v_1, \ell_2, v_3, r, \varpi, J\} - \min_{J'} E\{v_1, \ell_2, v_3, r, \varpi, J'\}, \quad (4)$$

118

$$E^{\nu_3}\{v_1, \ell_2, v_3, r, \varpi, J\} = \min_{J'} E\{0, 0, v_3, 1, e, J'\}, \quad (5)$$

119

$$E^{\nu_{12}}\{v_1, \ell_2, v_3, r, \varpi, J\} = \min_{J'} E\{v_1, \ell_2, v_3, r, \varpi, J'\} - E^{\nu_3}\{v_1, \ell_2, v_3, r, \varpi, J\}, \quad (6)$$

120 where $(v_1, \ell_2, v_3, r, \varpi, J)$ are the quantum numbers used in HITEMP-
 121 2010 to identify the rovibrational levels k . v_1 and v_3 are quantum numbers
 122 associated respectively with the vibrational modes ν_1 and ν_3 ; ℓ_2 is associated
 123 with the vibrational angular momentum of mode ν_2 ; the triplet (v_1, ℓ_2, v_3)
 124 enables to identify the Fermi polyad to which the level k belongs; r is the
 125 index of the vibrational level associated to the level k among the $v_1 + 1$
 126 vibrational levels constituting the Fermi polyad, ϖ is the parity (e or f) and
 127 J is the total angular momentum quantum number excluding nuclear spin of
 128 the level k . The populations of the few non-identified levels (0.9% of the lines
 129 as discussed in Sec. 2.3) have been calculated assuming LTE at temperature
 130 T . $Z_I(T, T_{12}, T_3)$ in Eq.(3) is the three-temperature partition function of the
 131 isotopologue I , which has been calculated using the approximation of the
 132 three uncoupled harmonic oscillators associated with the vibrational modes of
 133 CO_2 and of the rigid rotor, whose accuracy was demonstrated at equilibrium

134 for the main isotopologue in Ref. [27].¹ $Z_I(T, T_{12}, T_3)$ is given by:

$$Z_I(T, T_{12}, T_3) = \frac{k_b T}{\alpha_I B_I} \times \frac{1}{1 - \exp(-\omega_{1I}/k_b T_{12})} \frac{1}{[1 - \exp(-\omega_{2I}/k_b T_{12})]^2} \frac{1}{1 - \exp(-\omega_{3I}/k_b T_3)} \quad (7)$$

135 where B_I is the rotational constant of isotopologue I , $\alpha_I = 1$ or 2 depending
 136 on the isotopologue symmetry, ω_{1I} , ω_{2I} and ω_{3I} are the vibration energies
 137 associated with the three fundamental vibration modes taken for the differ-
 138 ent isotopologues from [28].

139

140 The models and data presented here are used to perform LBL calculations
 141 for building vibrational nonequilibrium SNB models for CO₂ in Doppler, and
 142 Lorentz broadening regimes. The Voigt broadening regime will be recov-
 143 ered using a mixing approach (see below), whose validation will also require
 144 LBL calculations in the Voigt regime. In the following, all calculations were
 145 achieved for a CO₂-N₂ mixture with a molar fraction $x_{\text{CO}_2} = 0.5$ using the
 146 input parameters provided in Table 1.

¹Under NLTE conditions, comparison of this uncoupled approach to a direct sum-
 mation on the identified levels of HITEMP-2010, using the splitting energy scheme of
 Eqs.(4-6), has been carried out on a regular 3D (T_{12}, T_3, T) temperature grid covering the
 domain $[500, 3000 \text{ K}] \times [500, 3000 \text{ K}] \times [500, 3000 \text{ K}]$ with a 100 K temperature step: devi-
 ations between the two approaches exhibit a root mean square value of 1.14% despite the
 incompleteness of HITEMP-2010 identified levels.

broadening regime	resolution [cm ⁻¹]	line wing cut-off [cm ⁻¹]	spectral domain [cm ⁻¹]
Lorentz	10 ⁻²	50	[237.5, 8312.5]
Doppler	10 ⁻³	10	[237.5, 8312.5]
Voigt	10 ⁻³	50	[237.5, 8312.5]

Table 1: Input parameters for the LBL calculations

147 *2.2. Spectral correlation issues*

148 The radiative transfer equation (RTE) along a line of sight in nonscattering
149 media is given by

$$\frac{dI_\sigma(s)}{ds} = \eta_\sigma(s) - \kappa_\sigma(s)I_\sigma(s), \quad (8)$$

150 where $I_\sigma(s)$ is the radiative intensity at the abscissa s along the line of sight.
151 The absorption and emission coefficients must be calculated beforehand to
152 solve this equation. This section aims to develop an RTE formulation un-
153 der nonequilibrium conditions suitable for applying statistical narrow-band
154 models. From Eq.(8), we can express the intensity escaping from a column
155 $(0,s)$ at s as:

$$I_\sigma(s) = \int_0^s \eta_\sigma(s')\tau_\sigma(s',s) ds', \quad (9)$$

156 where $\tau_\sigma(s',s) = \exp(-\int_{s'}^s \kappa_\sigma(s'')ds'')$ is the transmissivity of the column
157 (s',s) and $I_\sigma(s=0)$ is assumed equal to 0.

158

159 To use SNB models for solving the RTE, we must express the intensity av-
160 eraged over the spectral band $\Delta\sigma$. However, the emission coefficient η_σ and
161 the transmissivity τ_σ are strongly correlated. To correctly account for self-

162 correlation, the intensity averaged over the spectral band $\Delta\sigma$ is expressed
 163 as

$$\overline{I}_\sigma^{\Delta\sigma}(s) = \int_0^s \overline{\frac{\eta_\sigma}{\kappa_\sigma}(s') \frac{\partial \tau_\sigma}{\partial s'}(s',s)}^{\Delta\sigma} ds'. \quad (10)$$

164 To compute Eq. (10) with SNB models, a further simplification is necessary,
 165 which is

$$\overline{I}_\sigma^{\Delta\sigma}(s) \approx \int_0^s \overline{\left(\frac{\eta_\sigma}{\kappa_\sigma}(s')\right)}^{\Delta\sigma} \frac{\partial \overline{\tau}_\sigma^{\Delta\sigma}}{\partial s'}(s',s) ds' \quad (11)$$

166 assuming that $\frac{\eta_\sigma}{\kappa_\sigma}$ and $\frac{\partial \tau_\sigma}{\partial s'}$ are not correlated. This assumption is valid
 167 in LTE conditions because the ratio $\frac{\eta_\sigma}{\kappa_\sigma}$ is equal to the Planck's function
 168 $I_\sigma^0(T)$. However, it is not guaranteed in NLTE conditions since Kirchhoff's
 169 law is no longer valid and the ratio $\frac{\eta_\sigma}{\kappa_\sigma}$ can present important spectral dy-
 170 namics. Figure 1 presents two nonequilibrium conditions: an imbalance be-
 171 tween vibrational and rotational degrees of freedom with local equilibrium
 172 between vibrational modes (right) and an imbalance between both rotation
 173 and different vibrational modes (left). It is clear that the ratio follows neither
 174 Planck's function at temperature T_{12} nor Planck's function at temperature
 175 T_3 as shown in Fig.1 (left). The spectral dynamics are then more important
 176 than for rotation-vibration nonequilibrium, as shown in Fig.1 (right) and in
 177 [19]. Comparing $\overline{\eta_\sigma^{\Delta\sigma}}$ to $\overline{\eta_\sigma/\kappa_\sigma}^{\Delta\sigma} \times \overline{\kappa_\sigma^{\Delta\sigma}}$ is the most critical test to check the
 178 decorrelation assumption. Indeed, the expression of the intensity averaged
 179 over the spectral band $\Delta\sigma$ exiting of uniform column of length l considering
 180 the decorrelation assumption is given by :

$$\overline{I}_\sigma^{\Delta\sigma}(0 \rightarrow l) = \int_0^l \overline{\left(\frac{\eta_\sigma}{\kappa_\sigma}\right)}^{\Delta\sigma} \frac{\partial \overline{\tau}_\sigma^{\Delta\sigma}}{\partial s'}(s',l) ds' = \overline{\left(\frac{\eta_\sigma}{\kappa_\sigma}\right)}^{\Delta\sigma} (1 - \overline{\tau}_\sigma^{\Delta\sigma}(0 \rightarrow l)). \quad (12)$$

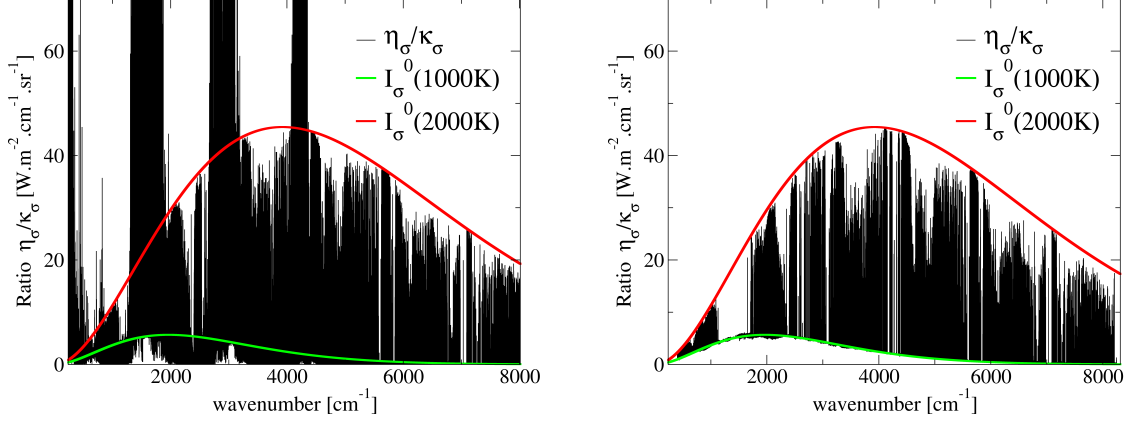


Figure 1: LBL $\eta_\sigma/\kappa_\sigma$ spectrum for $p = 1000$ Pa, $T = 2000$ K, $T_{12} = 1000$ K, $T_3 = 300$ K (left) and $p = 1000$ Pa, $T = 2000$ K, $T_{12} = 1000$ K, $T_3 = 1000$ K (right).

181 The spectral dynamics of the emissivity $1 - \tau_\sigma(0 \rightarrow l)$ is maximum when the
 182 medium is optically thin because the exponential function does not smooth
 183 the absorption coefficient spectral structures. The expression of the radiative
 184 intensity is, considering the decorrelation hypothesis, equal to

$$\overline{I_\sigma^{\Delta\sigma}}(0 \rightarrow l) \underset{\kappa_\sigma l \rightarrow 0}{=} \left(\frac{\eta_\sigma}{\kappa_\sigma} \right)^{\Delta\sigma} \overline{\kappa_\sigma^{\Delta\sigma}} l, \quad (13)$$

185 which explains the choice of comparing $\overline{\eta_\sigma^{\Delta\sigma}}$, the exact result, to $\overline{\eta_\sigma/\kappa_\sigma}^{\Delta\sigma} \times$
 186 $\overline{\kappa_\sigma^{\Delta\sigma}}$ for verifying the decorrelation assumption. These tests were performed
 187 for realistic strong nonequilibrium conditions. It turns out that the decorre-
 188 lation assumption between $\eta_\sigma/\kappa_\sigma$ and κ_σ is not valid for cases with a strong
 189 imbalance between the temperatures T_{12} and T_3 and a pressure $p \leq 10^4$ Pa, as
 190 shown in Fig. 2 (left). The influence of pressure on spectral dynamics is well
 191 known. Indeed, the line widths for Lorentz broadening regime are propor-
 192 tional to the pressure. Thus, decreasing the pressure increases the spectral

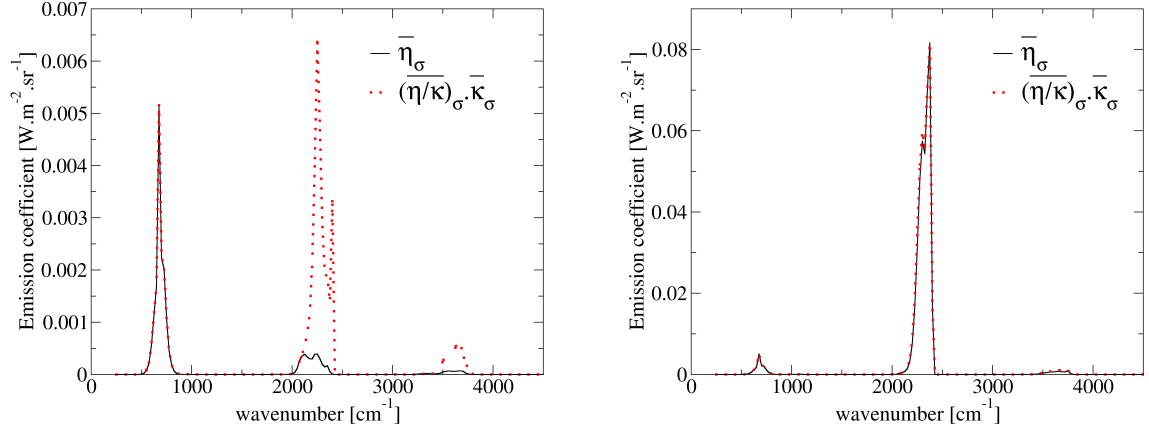


Figure 2: Comparison between $\overline{\eta_\sigma}^{\Delta\sigma}$ and $\overline{\eta_\sigma/\kappa_\sigma}^{\Delta\sigma} \times \overline{\kappa_\sigma}^{\Delta\sigma}$ for $p = 1000$ Pa, $T = 2000$ K, $T_{12} = 1000$ K, $T_3 = 300$ K (left) and $p = 1000$ Pa, $T = 2000$ K, $T_{12} = 1000$ K, $T_3 = 1000$ K (right); $x_{\text{CO}_2} = 0.5$.

193 dynamics and, therefore, the spectral correlation between $\eta_\sigma/\kappa_\sigma$ and κ_σ . Nev-
 194 ertheless, more than pressure's influence is needed to explain these spectral
 195 correlations since the decorrelation assumption is always verified at LTE. It
 196 combines being in both moderate pressure conditions and a strong imbalance
 197 between the two vibration temperatures. Fig. 2 (left) shows that the corre-
 198 lation issue arises only for the $2.7 \mu\text{m}$ and $4.3 \mu\text{m}$ bands. To understand
 199 further why these spectral bands are problematic under these conditions,
 200 high-resolution spectra of κ_σ and η_σ under the strong vibrational imbalance
 201 condition of Fig.2 (left part) have been plotted in Fig. 3 (lower and middle
 202 part of the figure), for a very narrow spectral range $[2247.62, 2247.69] \text{ cm}^{-1}$
 203 belonging to a problematic narrow-band identified in Fig.2. In the upper
 204 part of Fig. 3 are also plotted both $\eta_\sigma/\kappa_\sigma$ and again κ_σ , using a logarithmic
 205 scale, exhibiting a strong anticorrelation between κ_σ and $\eta_\sigma/\kappa_\sigma$: in this re-

206 gion, the absorption spectrum is dominated by vibrational transitions of the
 207 type $\Delta v_3 = 1$ near 2247.63 and 2247.675 cm^{-1} as mentioned in the lowest
 208 part of the figure; these transitions also contribute to the emission spectrum
 209 near the same spectral locations, but transitions of type $(\Delta v_1 = 1, \Delta \ell_2 = 1)$
 210 also contribute to the emission spectrum near 2247.655 cm^{-1} as indicated
 211 on the middle part of Fig. 3.² Each of these types of vibrational transitions,
 212 considered as an isolated line ($u - l$), will be characterized by very different
 213 values of the ratio $(\eta_\sigma/\kappa_\sigma)_{ul}$, whose general expression is

$$\left(\frac{\eta_\sigma}{\kappa_\sigma}\right)_{ul} = \frac{2hc\sigma_{ul}^3}{\exp\left(\frac{\Delta E_{ul}^{\nu_{12}}}{k_B T_{12}} + \frac{\Delta E_{ul}^{\nu_3}}{k_B T_3} + \frac{\Delta E_{ul}^{rot}}{k_B T}\right) - 1}. \quad (14)$$

214 In the above equation, $\Delta E_{ul}^{\nu_{12}}$, $\Delta E_{ul}^{\nu_3}$, and ΔE_{ul}^{rot} designate the energy varia-
 215 tion associated to resp. vibrational mode 12, vibrational mode 3, and rotation
 216 for the transition ul . For the two types of vibrational transitions identified
 217 above, resp. $\Delta v_3 = 1$ and $(\Delta v_1 = 1, \Delta \ell_2 = 1)$, the transition energy $hc\sigma_{ul}$ is
 218 mainly defined resp. by $\Delta E_{ul}^{\nu_3}$ and $\Delta E_{ul}^{\nu_{12}}$, while the rotational contribution
 219 $\Delta E_{ul}^{rot}/(k_B T)$ inside the exponential in Eq. (14) is negligible in comparison
 220 with vibrational one at $T = 2000$ K; the associated ratios $(\eta_\sigma/\kappa_\sigma)_{ul}$ may be

²Let note that about 16 rovibrational transitions are required to accurately model the spectra shown in Fig. 3: to simplify the analysis, only three dominant vibrational transitions have been mentioned near the local maximum of the spectra.

221 therefore approximated according to

$$\left(\frac{\eta_\sigma}{\kappa_\sigma}\right)_{\Delta v_3=1} \approx \frac{2hc\sigma_{ul}^3}{\exp\left(\frac{hc\sigma_{ul}}{k_B T_3}\right) - 1}, \quad (15)$$

$$\left(\frac{\eta_\sigma}{\kappa_\sigma}\right)_{\Delta v_1=1, \Delta \ell_2=1} \approx \frac{2hc\sigma_{ul}^3}{\exp\left(\frac{hc\sigma_{ul}}{k_B T_{12}}\right) - 1}, \quad (16)$$

222 and will be very different from each other in the condition ($T_3 = 300$ K,
 223 $T_{12} = 2000$ K) considered here. Although the overlapping between lines,
 224 especially at not too low pressures, should moderate this analysis (the ab-
 225 sorption coefficient near 2247.655 cm^{-1} is dominated by the line wings of the
 226 transitions $\Delta v_3 = 1$ even at 1000 Pa), the variability of the $(\eta_\sigma/\kappa_\sigma)_{ul}$ val-
 227 ues of the various contributing transitions to emission or absorption spectra
 228 explains the anticorrelation between κ_σ and $\eta_\sigma/\kappa_\sigma$ observed in Fig. 3, and
 229 thus the overestimation of the emission observed in Fig.2 (left) when using
 230 the decorrelation hypothesis Eq. 13. It is quite obvious from Eq. 14 that the
 231 variability of $(\eta_\sigma/\kappa_\sigma)_{ul}$ values will occur under strong vibrational disequilib-
 232 rium among vibrational transitions of different nature, viz. characterised by
 233 very different vibrational energy variations ($\Delta E_{ul}^{\nu_3}, \Delta E_{ul}^{\nu_{12}}$). Grouping tran-
 234 sitions into classes of similar vibrational energy variations will reduce the
 235 variability of $(\eta_\sigma/\kappa_\sigma)_{ul}$ inside each class and, therefore, improve the accuracy
 236 of the decorrelation approximation Eq. 13 when applied to the lines of a given
 237 class. Let note that the good behaviour of this decorrelation assumption in
 238 the $15 \mu\text{m}$ region (see Fig. 2) is consistent with the above analysis since in this
 239 spectral region, vibrational transitions involving only the mode (ν_1, ν_2) are
 240 dominant. Also, it is interesting to notice that a vibrational nonequilibrium
 241 with $T_3 > T_{12}$ does not introduce correlation issues in the main absorption

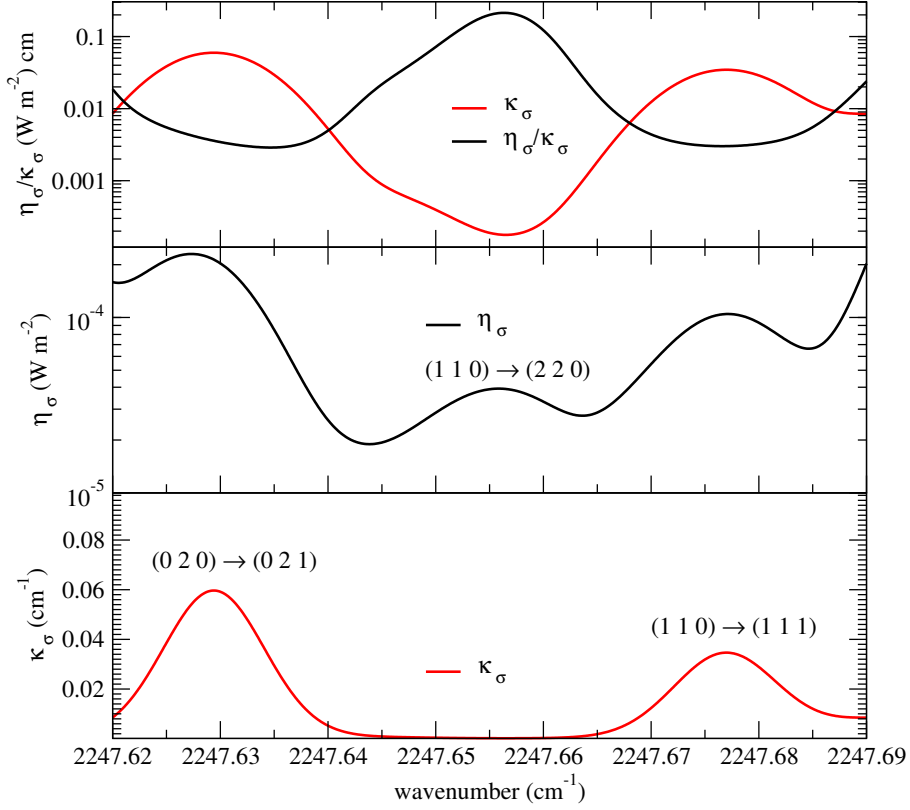


Figure 3: Absorption (κ_σ) and emission (η_σ) spectra of a CO₂-N₂ mixture at $T = 2000$ K, $T_{12} = 1000$ K, $T_3 = 300$ K, $p = 1000$ Pa, $x_{\text{CO}_2} = 0.5$. Typical dominant vibrational transitions (see footnote 2) are indicated near each local maximum of the spectra using the notation $(v_1 \ell_2 v_3)'' \rightarrow (v_1 \ell_2 v_3)'$ to designate lower '' and upper ' vibrational states. The upper part of the figure exhibits the anticorrelation between $\eta_\sigma/\kappa_\sigma$ and κ_σ for this strong vibrational imbalance condition.

242 bands near 4.3 and $2.7 \mu\text{m}$ since both emission and absorption spectra are
 243 dominated by $\Delta v_3 = 1$ transitions in this case.

244 *2.3. Definition of line classes*

245 Considering that the fundamental vibrational energies of mode ν_1 and ν_2
 246 approximately satisfy $\omega_{1I} \approx 2\omega_{2I}$ for each isotopologue I , the more accurate
 247 approach to ensure the decorrelation assumption's validity would consist of
 248 grouping the lines into classes according to the different observed values of
 249 $(2\Delta\nu_1 + \Delta\ell_2, \Delta\nu_3)$. Such an approach would lead to the introduction of
 250 more than 20 classes leading to a quite tedious model. Observing that in
 251 the two main spectral regions where CO₂ radiation has to be accounted for
 252 and where correlation issues arise, i.e. the 4.3 μm and the 2.7 μm regions,
 253 the main vibrational transitions satisfy $\Delta\nu_3 = 1$, it appears quite natural to
 254 split the database into lines satisfying $\Delta\nu_3 = 1$ or $\Delta\nu_3 \neq 1$. Table 2 presents
 255 the different line classes that have been defined and the distribution of the
 256 transitions per class.

name	ν_3	<i>not_ν3</i>	<i>not_defined</i>
definition	$\Delta\nu_3 = (\nu_3)' - (\nu_3)'' = 1$	$\Delta\nu_3 \neq 1$	$r' = 0$ or $r'' = 0$
proportion of lines	4554364 (40.9%)	6482107 (58.2%)	99692 (0.9%)

Table 2: Line classes for CO₂

257

258 The ν_3 and *not_ν3* classes represent more than 99% of the database lines. The
 259 class *not_defined* contains the lines for unknown upper or lower vibrational
 260 energy levels. It seems natural to consider these lines separately because we
 261 cannot use vibrational temperatures to predict the population of their asso-
 262 ciated upper or lower levels; that is why these level populations are assumed
 263 to follow a Boltzmann distribution at the translation/rotation temperature

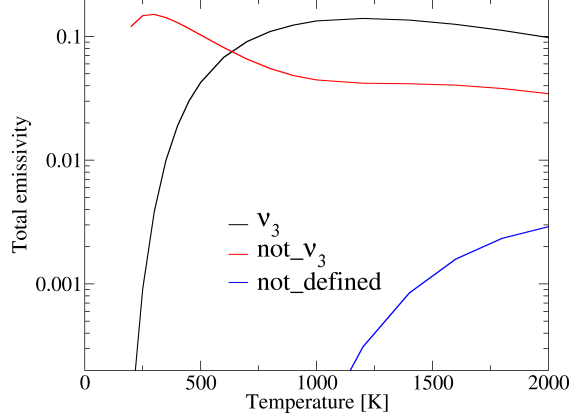


Figure 4: Comparison of emissivities of the three classes vs temperature at LTE for $p = 100000$ Pa, $l = 1$ m and $x_{\text{CO}_2} = 0.5$.

264 T . To evaluate the contribution of each class to the gas radiative properties,
 265 a comparison of the total emissivity of each class as a temperature function
 266 (at LTE) is plotted in Fig. 4. The total emissivity is computed following

$$\epsilon_{tot,class}(x_{\text{CO}_2}, p, l, T) = \frac{\pi}{\sigma_{SB} T^4} \sum_{bands\ b} (1 - \bar{\tau}_b^{\Delta\sigma}(x_{\text{CO}_2}, p, l, T)) \bar{I}_b^{\Delta\sigma}(T) \Delta\sigma, \quad (17)$$

267 where σ_{SB} is the Stefan-Boltzmann constant and I^0 is Planck's function. The
 268 ν_3 class ($\Delta\nu_3 = 1$) is the one that contributes the most above $T=700$ K, and
 269 the not_nu_3 class ($\Delta\nu_3 \neq 1$) is dominant below. As expected, the contribution
 270 of the $not_defined$ class is weak compared to the other classes.

271

272 Henceforth, a check for the validity of the decorrelation assumption is per-
 273 formed for each class. The one for the $not_defined$ class is useless because
 274 level populations for these lines are assumed at LTE. Fig.5 shows that split-
 275 ting into line classes solves the spectral correlation issue between $\eta_\sigma/\kappa_\sigma$ and

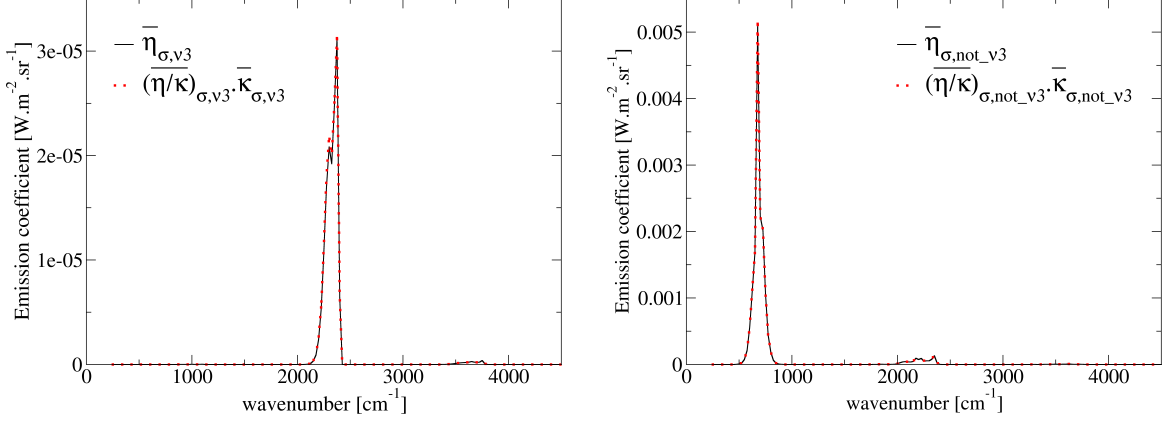


Figure 5: Emission coefficient for $\nu 3$ class (left) and not- $\nu 3$ class (right) for $p = 1000$ Pa, $T = 2000$ K, $T_{12} = 1000$ K, $T_3 = 300$ K, and $x_{\text{CO}_2} = 0.5$.

276 κ_σ . The formulation of the RTE equation, averaged over $\Delta\sigma$, with the multi-
 277 class approach for CO_2 is expressed following Lamet et al. [19], as :

$$\bar{I}_\sigma^{\Delta\sigma}(l) = \sum_{j=1}^{N_{\text{class}}} \int_0^l \overline{\left(\frac{\eta_\sigma}{\kappa_\sigma}\right)}_j^{\Delta\sigma}(s) \frac{\partial \bar{\tau}_j^{\Delta\sigma}}{\partial s}(s,l) \prod_{j' \neq j} \bar{\tau}_{j'}^{\Delta\sigma}(s,l) ds, \quad (18)$$

278 where a decorrelation assumption between classes has been used. The validity
 279 of this assumption is checked in Fig.6 and shows that the product of the
 280 transmissivities is indeed very close to the total transmissivity $\bar{\tau}_\sigma^{\Delta\sigma}$ of CO_2 .

281 2.4. Statistical narrow band model parameters

282 Equation (18) shows that the model requires the computation of parameters
 283 $\overline{(\eta_\sigma/\kappa_\sigma)}_j^{\Delta\sigma}$ and of transmissivities. The parameters $\overline{(\eta_\sigma/\kappa_\sigma)}_j^{\Delta\sigma}$ were directly
 284 tabulated from LBL calculations, and were found to be insensitive to line
 285 broadening regime. For transmissivities, the random SNB model of Mayer
 286 and Goody [29] has been selected in this study since it provides accurate

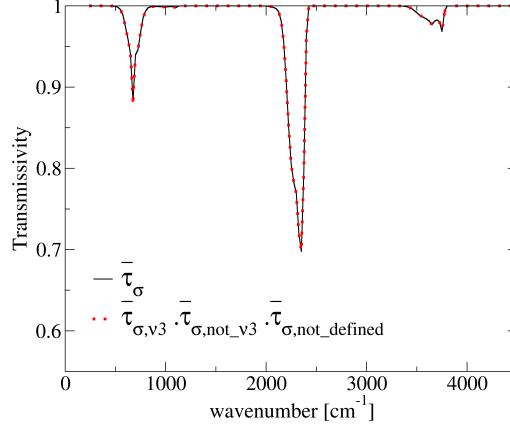


Figure 6: Comparison of the transmissivity product of each class with the total transmissivity, for $p = 1000$ Pa, $T = 2000$ K, $T_{12} = 1000$ K, $T_3 = 300$ K, $x_{\text{CO}_2} = 0.5$ and a column length $l = 1$ m .

287 results for polyatomic molecules at LTE. This model is based on statistical
 288 assumptions concerning line positions and intensities within a narrow band
 289 of width $\Delta\sigma$ and allows to express the transmissivity of a uniform column of
 290 length l , averaged over $\Delta\sigma$ as

$$\bar{\tau}^{\Delta\sigma}(l) = \frac{1}{\Delta\sigma} \int_{\Delta\sigma} \exp(-\kappa_\sigma l) d\sigma = \exp\left(-\frac{\bar{W}}{\delta}\right), \quad (19)$$

291 where $\delta = \Delta\sigma/N$ is the mean spacing between the N line positions within
 292 $\Delta\sigma$, and \bar{W} is the mean black equivalent width of these lines, defined as

$$\bar{W} = \frac{1}{N} \sum_{r=1}^N \int_{-\infty}^{+\infty} [1 - \exp(-\kappa_\sigma^r l)] d\sigma, \quad (20)$$

293 where κ_σ^r is the contribution of the r^{th} line to the absorption coefficient.
 294 Several line intensity distribution functions have been proposed to model
 295 \bar{W}/δ for Lorentz and Doppler line broadening. The most used are the Goody

296 exponential distribution [29], and the Malkmus tailed inverse-exponential
 297 distribution [30]. They are special cases (respectively for $\alpha = -1$ and $\alpha = 0$)
 298 of the generalized Malkmus distribution function of [31]. Its expression is the
 299 following

$$P_\alpha(S) : \frac{C_\alpha}{S} \left(\frac{S_m}{S} \right)^\alpha \left[\exp\left(-\frac{S}{S_m}\right) - \exp\left(-\frac{rS}{S_M}\right) \right], \quad (21)$$

300 where C_α is a normalization constant. In this study, the Malkmus distribu-
 301 tion function is used for the Lorentz broadening regime leading to

$$\frac{\overline{W}_L}{\delta} = \frac{2\overline{\gamma}_L}{\overline{\delta}_L} \left(\sqrt{1 + \frac{\overline{k}_L x_{\text{CO}_2} p l \overline{\delta}_L}{\overline{\gamma}_L}} - 1 \right). \quad (22)$$

302 In the Doppler broadening regime, P_α distribution leads to the mean equiv-
 303 alent line width expression

$$\frac{\overline{W}_D}{\delta} = \overline{\beta}_D H_\alpha\left(\frac{\overline{k}_D x_{\text{CO}_2} p l}{\overline{\beta}_D}\right) \quad (23)$$

304 with

$$H_\alpha(y) = \frac{1}{\alpha\sqrt{\pi}} \int_{-\infty}^{+\infty} [(1 + y \exp(-\xi^2))^\alpha - 1] d\xi \quad \text{for } \alpha \neq 0 \quad (24)$$

$$H_0(y) = \frac{1}{\sqrt{\pi}} \int_{-\infty}^{+\infty} \ln[1 + y \exp(-\xi^2)] d\xi \quad \text{for } \alpha = 0, \quad (25)$$

305 where $\overline{\delta}_L$ is a modified mean line spacing and $\overline{\beta}_D$ characterizes the degree of
 306 line overlapping. $\overline{k}_{L/D}$ is the reduced mean absorption coefficient and can be
 307 considered equal for the Lorentz and Doppler broadening regime ($\overline{k}_L = \overline{k}_D =$
 308 $\overline{k} = \overline{\kappa}_\sigma / (x_{\text{CO}_2} p)$) with good accuracy. The parameter $\overline{\gamma}_L$ represents the mean
 309 Lorentz half width at half maximum of the lines and is expressed for CO₂ as
 310 [32]

$$\overline{\gamma}_L = \frac{p}{p_s} \left(\frac{T_s}{T} \right)^{0.7} [0.07 x_{\text{CO}_2} + 0.058 (1 - x_{\text{CO}_2})], \quad (26)$$

311 where $p_s = 101,325$ Pa and $T_s = 296$ K.

312

313 For each broadening regime and each line class, parameters \bar{k} have been
314 obtained directly by averaging over each narrow band ($\Delta\sigma = 25$ cm⁻¹)
315 high-resolution absorption coefficients provided by LBL calculations based
316 on the HITEMP-2010 database. The parameters $\bar{\delta}_L$ and $\bar{\beta}_D$ have been gener-
317 ated from adjustments enabling the corresponding analytical expression of
318 $\overline{W_{L/D}/\delta}$, as a function of the column length l , to fit $-\ln(\bar{\tau}^{\Delta\sigma}(l))$ obtained
319 with LBL calculations (called the curve of growth). This adjustment is made
320 by minimizing the least square error thanks to the Newton method. The pa-
321 rameters $\bar{\delta}_L$ and \bar{k} are assumed independent of the pressure and are generated
322 at $p = 10^5$ Pa. For the curve of growth adjustments in the Lorentz broad-
323 ening regime, 20 transmissivities are prescribed from 0.02 to 0.95, and the
324 associated column lengths are computed from these transmissivities. For the
325 adjustments in Doppler broadening regime, 21 column lengths are provided
326 from $x_{\text{CO}_2}pl = 5$ Pa.m to $x_{\text{CO}_2}pl = 5000$ Pa.m with a regular logarithmic
327 step. Indeed, prescribing transmissivities near 0 for the Doppler broadening
328 regime would lead to huge and unrealistic column lengths. The parameter α
329 in the distribution function is equal to 0.3 excepted for narrow band centers
330 $\sigma = 2350/2375/2400$ cm⁻¹ where $\alpha = 0.2$. To quantify the errors introduced
331 by the SNB model for uniform columns, a mean quadratic error is defined

332 for the mean transmissivity $\bar{\tau}^{\Delta\sigma}$ as follows for each spectral band

$$s_\tau(\sigma) = \sqrt{\frac{1}{N_T \cdot N_{T_{12}} \cdot N_{T_3} \cdot N_l \cdot N_{class}}} \times \sqrt{\left(\sum_{i=1}^{N_T} \sum_{j=1}^{N_{T_{12}}} \sum_{k=1}^{N_{T_3}} \sum_{l=1}^{N_l} \sum_{n=1}^{N_{class}} \left((\bar{\tau}_{LBL}^{\Delta\sigma} - \bar{\tau}_{SNB}^{\Delta\sigma})(\sigma, T_i, T_{12,j}, T_{3,k}, l_l, class_n) \right)^2 \right)}, \quad (27)$$

333 and a relative mean quadratic error is defined for $1 - \bar{\tau}^{\Delta\sigma}$ for each spectral
334 band according to

$$s_{rel,1-\tau}(\sigma) = \sqrt{\frac{1}{N_T \cdot N_{T_{12}} \cdot N_{T_3} \cdot N_l \cdot N_{class}}} \times \sqrt{\left(\sum_{i=1}^{N_T} \sum_{j=1}^{N_{T_{12}}} \sum_{k=1}^{N_{T_3}} \sum_{l=1}^{N_l} \sum_{n=1}^{N_{class}} \left(\left(\frac{\bar{\tau}_{LBL}^{\Delta\sigma} - \bar{\tau}_{SNB}^{\Delta\sigma}}{1 - \bar{\tau}_{LBL}^{\Delta\sigma}} \right) (\sigma, T_i, T_{12,j}, T_{3,k}, l_l, class_n) \right)^2 \right)}, \quad (28)$$

335 where $N_T, N_{T_{12}}, N_{T_3}, N_{class}$ are the number of grid points of the variables
336 $T, T_{12}, T_3, class$, respectively, for which parameters have been obtained. For
337 the temperatures, the grid contains the 32 following values: [200, 250, 300,
338 350, 400, 450, 500, 600, 700, 800, 900, 1000, 1100, 1200, 1300, 1400, 1500,
339 1600, 1700, 1800, 1900, 2000, 2200, 2400, 2600, 2800, 3000, 3200, 3400,
340 3600, 3800, 4000]. The N_l lengths l correspond to the ones used to perform
341 the curve of growth adjustments of $\bar{\delta}_L$ and $\bar{\beta}_D$. These error estimators are
342 presented in Fig. 7 and Fig. 8 and show that the adjustment errors are
343 maximum when performed in the absorption bands, which is expected since
344 the curves of growth are linear for small optical thicknesses. The errors for

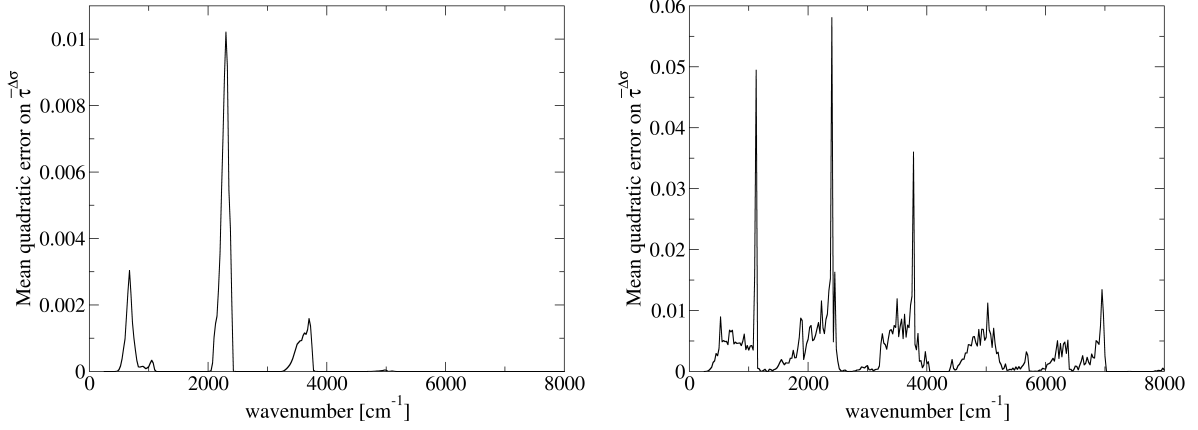


Figure 7: Mean quadratic error on $\bar{\tau}^{-\Delta\sigma}$ for Doppler broadening regime (left) and Lorentz broadening regime (right)

345 Lorentz broadening regime appear higher than for the Doppler regime. How-
 346 ever, transmissivities are prescribed in Lorentz broadening, which means that
 347 the adjustment is made for a wide range of optical thicknesses. Therefore,
 348 the errors displayed for Lorentz broadening involve contributions of all trans-
 349 missivity ranges, unlike for Doppler broadening, where errors are checked on
 350 the optically thin or medium part of the curve of growth.

351

352 In the context of high-altitude rocket plumes, we have to consider the Voigt
 353 broadening regime for which the mean black equivalent line width is calcu-
 354 lated by combining \overline{W}_L/δ and \overline{W}_D/δ expressions, according to the Ludwig
 355 formula

$$\frac{\overline{W}_V}{\delta} = \bar{k}x_{\text{CO}_2}pl\sqrt{1 - \Omega^{-1/2}} \quad \text{with}$$

$$\Omega = \left[1 - \left(\frac{1}{\bar{k}x_{\text{CO}_2}pl} \frac{\overline{W}_D}{\delta} \right)^2 \right]^{-2} + \left[1 - \left(\frac{1}{\bar{k}x_{\text{CO}_2}pl} \frac{\overline{W}_L}{\delta} \right)^2 \right]^{-2} - 1 \quad (29)$$

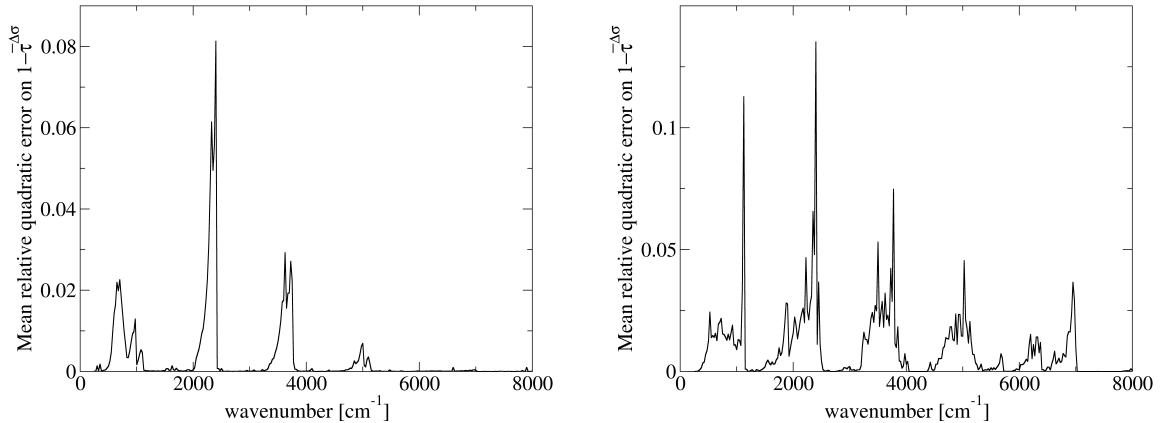


Figure 8: Mean relative quadratic error on $1 - \bar{\tau}^{\Delta\sigma}$ for Doppler broadening regime (left) and Lorentz broadening regime (right)

356 as proposed in [33].

357

358 To validate the SNB model in this regime, we compare the radiative intensity
 359 at the exit of a uniform column from the model expressed as Eq.(18) and
 360 the LBL approach for the nonequilibrium conditions considered in Fig. 2 in
 361 a wide range of pressure. This allows us to check the model in all broadening
 362 regimes and ensure that the mixing formula and the mixing of classes do not
 363 downgrade model accuracy. The comparison in Fig. 9 shows a good agree-
 364 ment between the SNB model and the LBL approach for the two conditions.

365

366 To conclude this subsection, the SNB parameters $\overline{(\eta_\sigma/\kappa_\sigma)^{\Delta\sigma}}$, \bar{k} , $\bar{\delta}_L$, and $\bar{\beta}_D$
 367 have been tabulated as function of the three temperatures T , T_{12} , and T_3 ,
 368 for each class and each narrow band. The temperature grid is the one given
 369 above. Note that the developed model can be easily extended to a four-

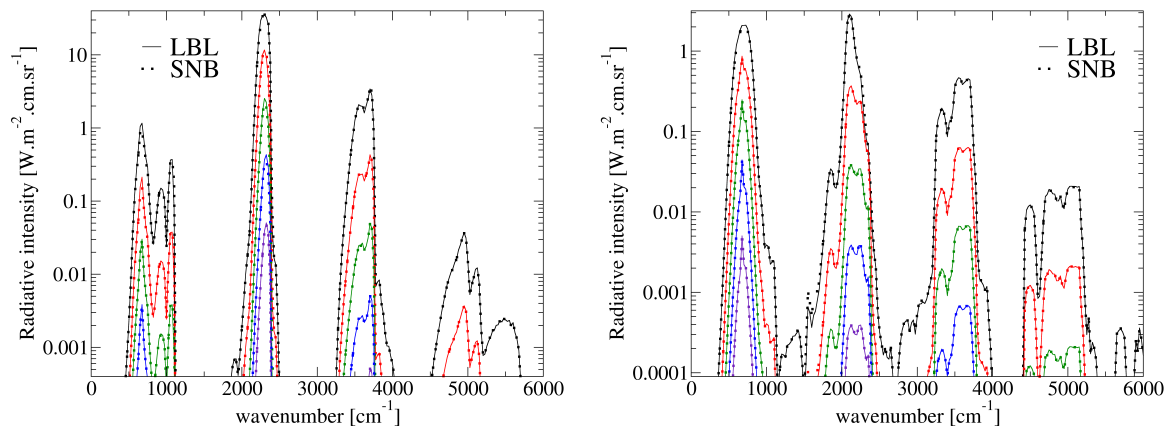


Figure 9: Radiative intensity for a uniform column at $l = 0.1$ m for $x_{\text{CO}_2} = 0.5$, $T = 300$ K, $T_{12} = 1000$ K, $T_3 = 2000$ K (left) and $l = 10$ m for $x_{\text{CO}_2} = 0.5$, $T = 2000$ K, $T_{12} = 1000$ K, $T_3 = 300$ K (right). The pressure is $p = 10000$ Pa (black), $p = 1000$ Pa (red), $p = 100$ Pa (green), $p = 10$ Pa (blue) and $p = 1$ Pa (indigo).

370 temperature model as the one developed in [34] where different temperatures
 371 are assigned to the symmetric stretching and the bending modes of CO_2 .
 372 Indeed, the line classes are chosen on the basis of vibrational transitions
 373 in the asymmetric stretching mode. Model parameters should be however
 374 tabulated versus the four temperatures T , T_1 , T_2 , and T_3 , and supplementary
 375 line classes could be required for strong differences between T_1 and T_2 .

376 3. Application to radiative transfer

377 This model aims to be applied in realistic radiative transfer calculations.
 378 It must, therefore, give satisfactory results for non-uniform columns. The
 379 radiative intensity at the exit of a non-uniform column with N_{col} sub-columns

380 indexed i from the multi-class SNB model is approximated by

$$\begin{aligned} \bar{I}^{\Delta\sigma}(N^+) &= \sum_{j=1}^{N_{class}} \sum_{i=1}^{N_{col}} \overline{\left(\frac{\eta_\sigma}{\kappa_\sigma}\right)}_j^{\Delta\sigma} (T^i, T_{12}^i, T_3^i) \times \\ &\quad \left[\overline{\tau}_j^{\Delta\sigma}(i^+ \rightarrow N^+) - \overline{\tau}_j^{\Delta\sigma}(i^- \rightarrow N^+) \right] \sqrt{\prod_{j' \neq j} \overline{\tau}_{j'}^{\Delta\sigma}(i^+ \rightarrow N^+) \prod_{j' \neq j} \overline{\tau}_{j'}^{\Delta\sigma}(i^- \rightarrow N^+)}, \end{aligned} \quad (30)$$

381 where $+$ and $-$ represent resp. the inlet and the outlet of the sub-column i .

382 The approximation is valid if each sub-column (i^-, i^+) is optically thin.

383

384 The Curtis-Godson (C-G) [35] and Lindquist-Simmons (L-S) [36, 37] ap-

385 proaches are the most commonly used formulations to express the mean

386 transmissivity for non-uniform columns with SNB models. In the Curtis-

387 Godson formulation, it is assumed that the mean transmissivity of a non-

388 uniform column, bounded by abscissae 0 and l , may be expressed similarly

389 to Eq.(19)

$$\overline{\tau}_{CG}^{\Delta\sigma}(0, l) = \exp\left(-\frac{\overline{W}^{CG}}{\delta}(0, l)\right). \quad (31)$$

390 For the Lorentz broadening regime, the mean black equivalent width is given

391 by

$$\frac{\overline{W}_L^{CG}}{\delta} = \frac{\overline{\beta}_L^*}{\pi} \left(\sqrt{1 + \frac{2\pi u^* \overline{k}^*}{\beta_L^*}} - 1 \right), \quad (32)$$

392 where u^* , $\overline{\beta}_L^*$ and \overline{k}^* are the effective parameters defined as

$$u^* = \int_0^l x_{\text{CO}_2}(s) p(s) ds, \quad (33)$$

393

$$\overline{k}^* u^* = \int_0^l x_{\text{CO}_2}(s) p(s) \overline{k}(s) ds, \quad (34)$$

394

$$\overline{\beta}_L^* = \frac{1}{k^* u^*} \int_0^l x_{\text{CO}_2}(s) p(s) \overline{k}(s) 2\pi \frac{\overline{\gamma}_L}{\delta_L}(s) ds. \quad (35)$$

395 The Curtis-Godson formulation for the Doppler broadening regime is ex-
 396 pressed as

$$\frac{\overline{W}_D^{CG}}{\delta} = \overline{\beta}_D^* H_\alpha \left(\frac{u^* \overline{k}^*}{\overline{\beta}_D^*} \right), \quad (36)$$

397 where $\overline{\beta}_D^*$ can be defined in the classical approach according to

$$\overline{\beta}_D^* = \frac{1}{\overline{k^* u^*}} \int_0^l x_{\text{CO}_2}(s) p(s) \overline{k}(s) \overline{\beta}_D(s) ds, \quad (37)$$

398 and in the formal approach leading to

$$\frac{1}{\overline{\beta}_D^*} = \frac{1}{\overline{k^* u^*}} \int_0^l x_{\text{CO}_2}(s) p(s) \overline{k}(s) \frac{1}{\overline{\beta}_D(s)} ds, \quad (38)$$

399 as provided in [19, 31]. The Lindquist–Simmons approaches provide approx-
 400 imate expressions of the path length derivative of the mean black equivalent
 401 width $\overline{W}(s, l)/\delta$ and is defined as follows in [31] for the Doppler and Lorentz
 402 broadening regimes

$$-\frac{1}{\delta} \frac{\partial \overline{W}_D^{LS}}{\partial s}(s, \ell) = \overline{k}(s) x_{\text{CO}_2}(s) p(s) y_\alpha \left(\frac{\overline{k}^*(s) u^*(s)}{\overline{\beta}_D^*(s)}, \frac{\overline{\beta}_D(s)}{\overline{\beta}_D^*(s)} \right), \quad (39)$$

403 with

$$y_\alpha(x, \rho) = \frac{1}{\sqrt{\pi}} \int_{-\infty}^{+\infty} \frac{e^{-\xi^2}}{[1 + x \exp(-\rho^2 \xi^2)]^{1-\alpha}} d\xi, \quad (40)$$

404 and

$$-\frac{1}{\delta} \frac{\partial \overline{W}_L^{LS}}{\partial s}(s, l) = x_{\text{CO}_2}(s) p(s) \overline{k}(s) y \left[\frac{\pi \overline{k}^*(s) u^*(s)}{\overline{\beta}_L^*(s)}, \frac{\overline{\beta}_L(s)}{\overline{\beta}_L^*(s)} \right]. \quad (41)$$

405 with

$$y(x, \rho) = \frac{2\rho(1+x) + (1+\rho^2)\sqrt{1+2x}}{\sqrt{1+2x}(\rho + \sqrt{1+2x})^2}, \quad (42)$$

406 and

$$\overline{\beta}_L(s) = 2\pi \frac{\overline{\gamma}_L}{\delta_L}(s). \quad (43)$$

407 As the formulation depends on the parameter $\overline{\beta_D^*}$, there are also classical and
408 formal approaches for the Lindquist-Simmons formulation in the Doppler
409 broadening regime.

410

411 To validate the developed SNB model, we consider four cases of non-uniform
412 columns representative of high-altitude plume applications. The first column
413 is a quasi-unidimensional expanding isentropic flow in a conical nozzle of
414 radius $R = 10$ cm at the throat and a cone angle of 15° . The flowing gas is a
415 non-reacting perfect mixture of N_2 - CO_2 - H_2O with respective molar fractions
416 of 70%, 20%, and 10%. The flow conditions at the throat are assumed to
417 be sonic (Mach number=1) with an initial LTE temperature $T_0 = 3000$ K, a
418 mass flow rate of $9 \text{ kg}\cdot\text{m}^{-2}\cdot\text{s}^{-1}$, leading to an initial velocity $u_0 = 1118 \text{ m}\cdot\text{s}^{-1}$.
419 More details about this case are given in [9]. Fig. 10 shows the pressure and
420 CO_2 temperature profiles during the quasi-unidimensional expansion. The
421 radiative intensity at the exit of the nozzle axis line of sight is computed
422 with the LBL and the SNB approaches and is compared in Fig. 11. We
423 can see that the L-S formal formulation gives the best result in the $15 \mu\text{m}$
424 band of CO_2 , but the C-G formal approximation is the most accurate one
425 for the $4.3 \mu\text{m}$ and $2.7 \mu\text{m}$ bands. To sum up, all the models are accurate
426 for this case and the mean relative errors for the bands presented here are
427 approximately 2%. For this case, the C-G formal approach seems to best
428 agree with the LBL approach if we consider the whole spectrum.

429

430 The second and third studied cases are non-uniform columns obtained thanks
431 to a Lagrangian post-processing method applied to LTE simulation of the

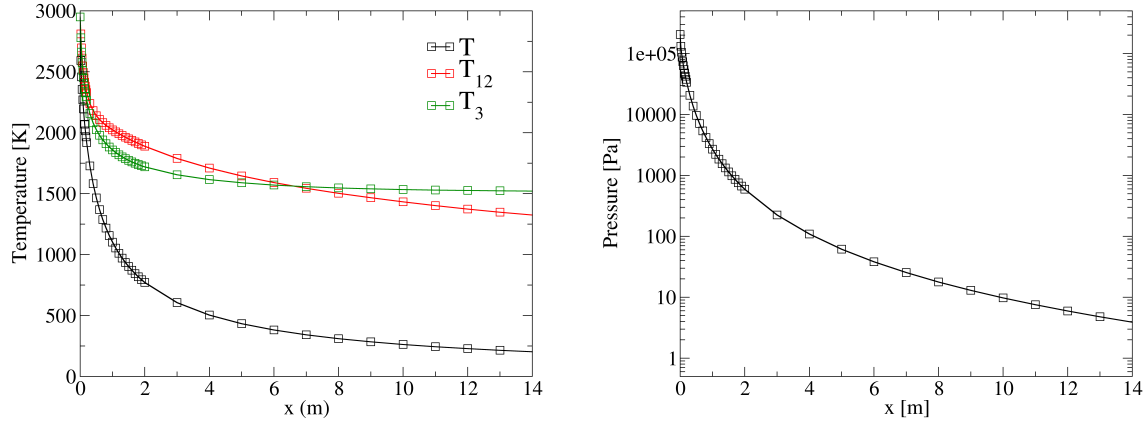


Figure 10: Temperature (left) and pressure (right) profiles of the quasi-unidimensional expanding nozzle flow from [9].

432 plume of the solid propellant motor Antares II from the "Bow Shock Ultra-
 433 violet2" (BSUV2) experiment [38]. This post-processing method was used
 434 on the LTE temperature field of the plume to determine all of the vibrational
 435 temperature fields. An exhaustive explanation of this method is presented in
 436 [9]. The first column considered is 20 m long, starting from the nozzle exit
 437 at $r/2$ from the plume axis of symmetry, where r is the nozzle radius at the
 438 nozzle exit and is parallel to the plume axis of symmetry. This case is called
 439 hereafter the axial column. The second line of sight called the transverse
 440 column, crosses the plume perpendicularly to its axis and intersects this axis
 441 at $x = 2$ m away from the nozzle exit. For these two columns, the molar frac-
 442 tion of CO_2 is $x_{\text{CO}_2} = 0.0136$. Pressure and temperature distributions along
 443 these columns are plotted in Fig.12 and Fig. 14. For the axial column, the
 444 L-S classical approach provides the best agreement with the LBL approach
 445 in Fig.13. For the transverse column, the L-S formal approach seems more

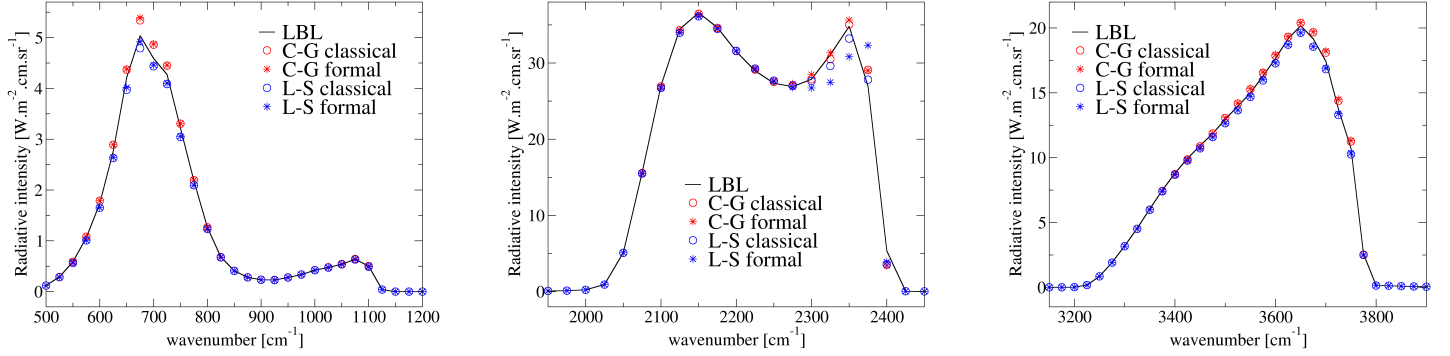


Figure 11: Radiative intensities at the exit of the nozzle axis line of sight in the 15 μm (left), 4.3 μm (middle) and 2.7 μm (right) regions of CO_2 for the quasi-unidimensional expanding flow.

446 accurate than the C-G approximation in Fig.15, but the difference is tight. It
 447 can be observed from Figs. 13 and 15 that more scatter between the different
 448 models is observed in the 4.3 μm region since this is the most optically thick
 449 region and the effects of the overlapping parameters $\bar{\beta}_{L/D}$ become the most
 450 important. For both columns, the mean relative errors remain limited to 3%
 451 whatever the considered model.

452

453 The last case is a non-uniform column representative of Mars entry condi-
 454 tions. It is a $\text{CO}_2\text{-N}_2$ mixture discretized in two uniform columns whose
 455 conditions are given in the table 3. The radiative intensity at the exit of
 456 the sub-column 2 in the direction $1 \rightarrow 2$ is computed with the SNB model
 457 and compared with LBL approach results. Although the HITEMP database
 458 might be inaccurate for temperatures around 3500 K, the purpose is to test
 459 the SNB model, not the database. It is clear in Fig. 16 that the classical
 460 Lindquist-Simmons approach is the most accurate for this case, with a mean

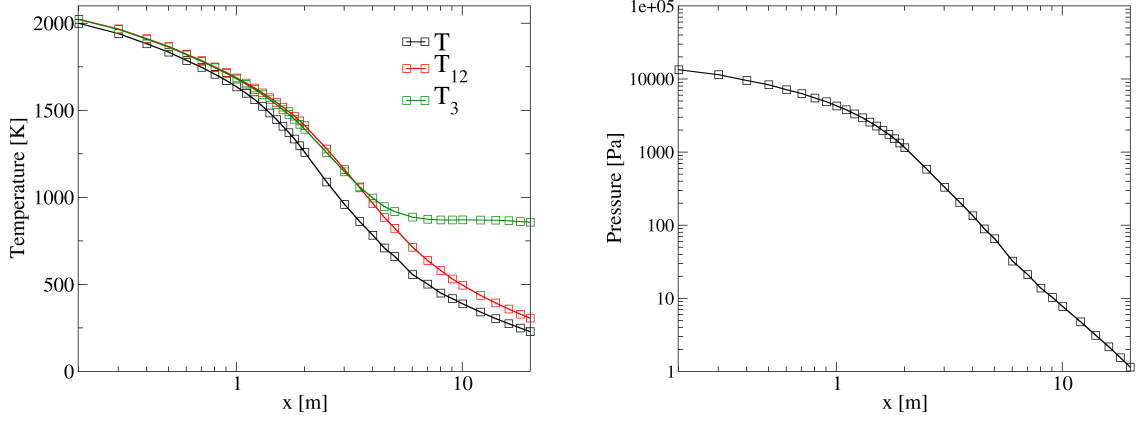


Figure 12: Temperature (left) and pressure (right) profiles of the axial column from [9].

element	p [Pa]	T [K]	T_{12} [K]	T_3 [K]	length [m]	x_{CO_2}
1	1000	3500	1500	700	0.05	0.6
2	500	3000	500	240	0.05	0.6

Table 3: Conditions of the non-uniform column representative of Mars entry conditions

461 relative error of about 2 % on the computed spectral intensity. The $2.7 \mu\text{m}$
 462 and $15 \mu\text{m}$ regions are optically thin, so the model degenerates in $\overline{k^*}$ in these
 463 bands. We can conclude that the developed nonequilibrium SNB model gives
 464 satisfactory results for both strong compression and expansion cases.

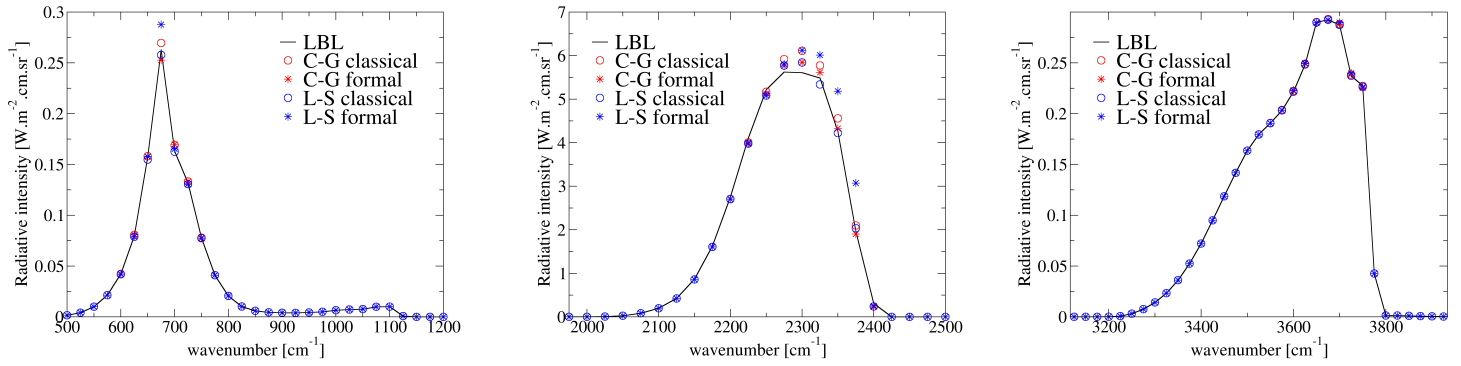


Figure 13: Radiative intensities at the exit of the axial column in the 15 μm (left), 4.3 μm (middle) and 2.7 μm (right) regions of CO_2 .

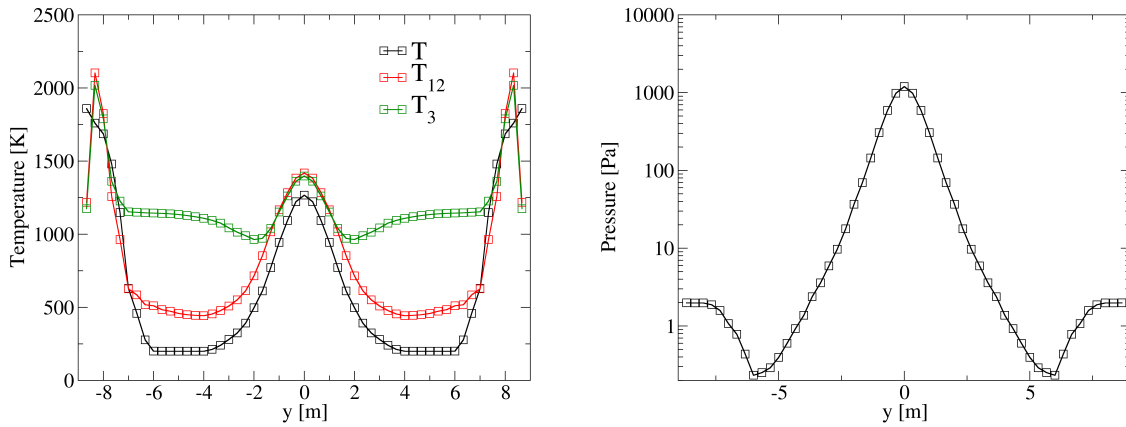


Figure 14: Temperature (left) and pressure (right) profiles of the transverse column from [9].

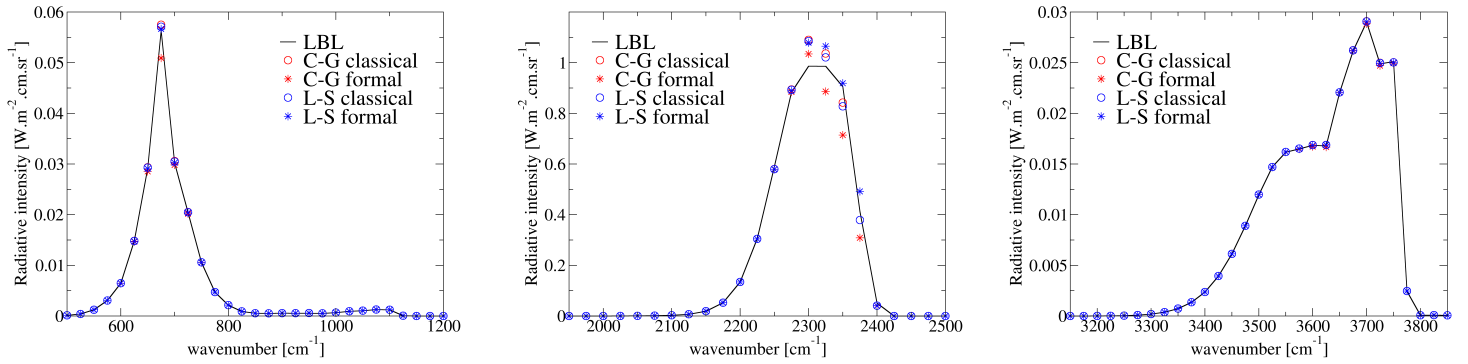


Figure 15: Radiative intensities at the exit of the transverse column in the $15 \mu m$ (left), $4.3 \mu m$ (middle) and $2.7 \mu m$ (right) regions of CO_2 .

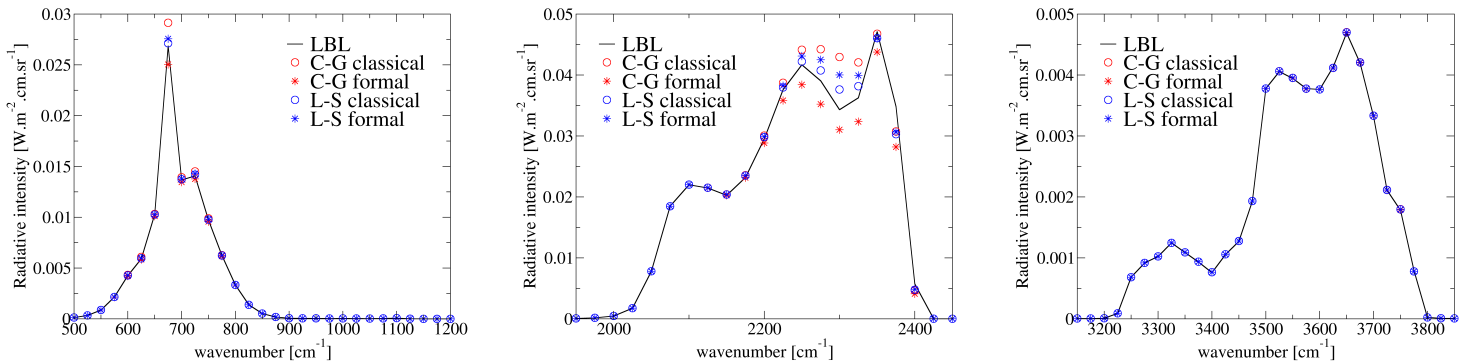


Figure 16: Radiative intensities at the exit of the line of sight in the direction $1 \rightarrow 2$ in the $15 \mu m$ (left), $4.3 \mu m$ (middle) and $2.7 \mu m$ (right) bands of CO_2 for the Mars entry representative conditions.

465 4. Conclusion

466 A vibrational nonequilibrium SNB model for CO₂ has been developed and
467 presented in this paper. The calculation of population densities is based
468 on a three-temperature approach (T, T_{12}, T_3) corresponding resp. to the
469 translational-rotational mode, the symmetric stretching and bending mode,
470 and the antisymmetric stretching mode. Since Kirchhoff's law is no longer
471 valid under these conditions, it is necessary to check the decorrelation be-
472 tween $\eta_\sigma/\kappa_\sigma$ and κ_σ beforehand. With these tests, we highlighted that there
473 are correlation issues between $\eta_\sigma/\kappa_\sigma$ and κ_σ in the 4.3 μm and 2.7 μm re-
474 gions of CO₂ for strong nonequilibrium between the temperatures T_{12} and
475 T_3 . This issue is caused by the proximity of transitions whose $\frac{\eta_\sigma}{\kappa_\sigma}$ ratio is
476 dominated by the T_{12} and the T_3 temperatures. The proposed solution was
477 to define classes of lines with similar vibrational transitions. SNB model
478 parameters were obtained by adjusting the curves of growth obtained from
479 the LBL approach for Lorentz and Doppler broadening regimes for each line
480 class. The quality of the adjustments was then discussed quantitatively us-
481 ing error statistics. Moreover, the SNB model accuracy was studied for the
482 Voigt broadening regime by comparing the radiative intensity escaping from
483 uniform columns for a wide pressure range in two strong nonequilibrium con-
484 ditions. This model was also applied for representative cases of high-altitude
485 expanding plumes and Mars entry conditions and showed satisfactory results.

486

487 **Acknowledgements**

488 The authors acknowledge the financial support of this study from the French
489 Agence de l'Innovation de Défense (AID). This work was granted access to the
490 HPC resources of IDRIS under the allocation 2022-A0102B00209 attributed
491 by GENCI (Grand Equipement National de Calcul Intensif). This work was
492 also performed using HPC resources from the Mésocentre computing center
493 of CentraleSupélec and Ecole Normale Supérieure Paris-Saclay supported by
494 CNRS and Région Île-de-France (<http://mesocentre.centralesupelec.fr/>).

495 **References**

- 496 [1] E. V. Kustova, E. A. Nagnibeda, Y. D. Shevelev, N. G. Syzranova,
497 Comparison of different models for non-equilibrium CO₂ flows in a shock
498 layer near a blunt body, *Shock waves* 111 (2011) 273–287.
- 499 [2] J.-M. Lamet, Y. Babou, Ph. Rivière, M.-Y. Perrin, A. Soufiani, Ra-
500 diative transfer in gases under thermal and chemical nonequilibrium
501 conditions: Application to earth atmospheric re-entry, *Journal of Quan-
502 titative Spectroscopy and Radiative Transfer* 109 (2008) 235–244.
- 503 [3] C. K. N. Patel, Continuous-Wave Laser Action on Vibrational-
504 Rotational Transitions of CO₂, *Physical Review* 136 (1964) 1187–1193.
- 505 [4] J. D. Anderson, *Gas Dynamic Lasers: An Introduction.*, Academic press,
506 1976.
- 507 [5] F. S. Simmons, *Rocket exhaust plume phenomenology*, The Aerospace
508 Press, 2000.
- 509 [6] I. Armenise, E. V. Kustova, Mechanisms of Coupled Vibrational Re-
510 laxation and Dissociation in Carbon Dioxide, *The Journal of Physical
511 Chemistry A* 122 (23) (2018) 5107–5120.
- 512 [7] V. Kotov, Two-modes approach to the state-to-state vibrational kinetics
513 of CO₂, *Journal of Physics B: Atomic, Molecular, and Optical Physics*
514 53 (2020).
- 515 [8] T. Kozac, A. Bogaerts, Evaluation of the energy efficiency of CO₂ con-

- 516 version in microwave discharges using a reaction kinetics model, Plasma
517 sources science and technology 24 (2015).
- 518 [9] Q. Binauld, Ph. Rivière, J.-M. Lamet, L. Tessé, A. Soufiani, CO₂ IR
519 radiation modelling with a multi-temperature approach in flows under
520 vibrational nonequilibrium, Journal of Quantitative Spectroscopy and
521 Radiative Transfer 239 (2019) 106652.
- 522 [10] E. V. Kustova, E. A. Nagnibeda, On a correct description of a multi-
523 temperature dissociating CO₂ flow, Chemical Physics 321 (2006) 293–
524 310.
- 525 [11] I. E. Gordon, L. S. Rothman, C. Hill, et al., The HITRAN2016 molec-
526 ular spectroscopic database, Journal of Quantitative Spectroscopy and
527 Radiative Transfer 203 (2017) 3–69.
- 528 [12] L. S. Rothman, I. E. Gordon, R. J. Barber, et al., HITEMP, the high-
529 temperature molecular spectroscopic database, Journal of Quantitative
530 Spectroscopy and Radiative Transfer 111 (2010) 2139–2150.
- 531 [13] S. A. Tashkun, V. I. Perevalov, CDS-4000: High-resolution, high-
532 temperature carbon dioxide spectroscopic databank, Journal of Quanti-
533 tative Spectroscopy and Radiative Transfer 112 (2011) 1403–1410.
- 534 [14] A. Bansal, M. F. Modest, D. A. Levin, Narrow-band k -distribution
535 database for atomic radiation in hypersonic nonequilibrium flows, in:
536 HT2009:Proceedings of the ASME summer heat transfer conference,
537 Vol. 1, 2009.

- 538 [15] A. Bansal, M. F. Modest, Multiscale Part-Spectrum k -distribution
539 database for atomic radiation in hypersonic nonequilibrium flows, Jour-
540 nal of Heat Transfer-transactions of the ASME 133 (12) (2011).
- 541 [16] A. Bansal, M. F. Modest, D. A. Levin, Multiscale k -distribution model
542 for gas mixtures in hypersonic nonequilibrium flows, Journal of Quanti-
543 tative Spectroscopy and Radiative Transfer 112 (7) (2011) 1213–1221.
- 544 [17] A. Sahai, C. O. Johnston, B. Lopez, M. Panesi, Comparative analy-
545 sis of reduced-order spectral models and grouping strategies for non-
546 equilibrium radiation, Journal of Quantitative Spectroscopy and Radia-
547 tive Transfer 242 (7) (2020).
- 548 [18] L. Pierrot, Ph. Rivière, A. Soufiani, J. Taine, A fictitious-gas-based
549 absorption distribution function global model for radiative transfer in
550 hot gases, Journal of Quantitative Spectroscopy and Radiative Transfer
551 62 (5) (1999) 609–624.
- 552 [19] J.-M. Lamet, Ph. Rivière, M.-Y. Perrin, A. Soufiani, Narrow-band model
553 for nonequilibrium air plasma radiation, Journal of Quantitative Spec-
554 troscopy and Radiative Transfer 111 (2010) 87–104.
- 555 [20] A. Sahai, C. O. Johnston, B. Lopez, M. Panesi, Flow-radiation coupling
556 in CO₂ hypersonic wakes using reduced-order non-Boltzmann models ,
557 Physical Review Fluids 4 (9) (2019).
- 558 [21] N. N. Kudriavtsev, S. S. Novikov, Theoretical and experimental investi-
559 gations of IR radiation transfer in vibrationally nonequilibrated molecu-

- 560 lar gas containing CO₂ and CO, International Journal of Heat and Mass
561 Transfer 25 (1982) 1541–1558.
- 562 [22] E. I. Vitkin, S. L. Shuralyov, V. V. Tamanovich, Radiation transfer in
563 vibrationally nonequilibrium gases, International Journal of Heat and
564 Mass Transfer 38 (1995) 163–173.
- 565 [23] E. I. Vitkin, V. G. Karelin, A. A. Kirillov, A. S. Suprun, J. V. Khadyka,
566 A physico-mathematical model of rocket exhaust plumes, International
567 Journal of Heat and Mass Transfer 40 (1997) 1227–1241.
- 568 [24] A. M. Molchanov, L. V. Bykov, D. S. Yanyshch, Calculating thermal
569 radiation of a vibrational nonequilibrium gas flow using the method of
570 *k*-distribution, Thermophysics and Aeromechanics 24 (2017) 399–419.
- 571 [25] G. Herzberg, Molecular spectra and molecular structure. II. Infrared
572 and Raman spectra of polyatomic molecules., Van Nostrand Company,
573 1956.
- 574 [26] J. Blauer, G. Nickerson, A survey of vibrational relaxation rate data for
575 processes important to CO₂-N₂-H₂O infrared plume radiation, in: AIAA
576 7th Fluid and Plasma Dynamics Conference, Palo Alto, California, June
577 17-19, AIAA paper 74-536, 1974.
- 578 [27] S. Depraz, M. Y. Perrin, P. Rivière, A. Soufiani, Infrared emission spec-
579 troscopy of CO₂ at high temperature. Part II: Experimental results and
580 comparisons with spectroscopic databases, Journal of Quantitative Spec-
581 troscopy and Radiative Transfer 113 (1) (2012) 14–25.

- 582 [28] A. Chedin, The carbon dioxide molecule: Potential, spectroscopic, and
583 molecular constants from its infrared spectrum, *Journal of Molecular*
584 *Spectroscopy* 76 (1979) 430–491.
- 585 [29] R. M. Goody, Y. L. Yung, *Atmospheric radiation*, 2nd Edition, Oxford
586 University Press, 1989.
- 587 [30] W. Malkmus, Random Lorentz Band Model with Exponential-Tailed
588 S^{-1} Line-Intensity Distribution Function, *Journal of the Optical Society*
589 *of America* 57 (1967) 323–329.
- 590 [31] Ph. Rivière, A. Soufiani, Generalized Malkmus line intensity distribution
591 for CO₂ infrared radiation in Doppler broadening regime, *Journal of*
592 *Quantitative Spectroscopy and Radiative Transfer* 112 (2011) 475–485.
- 593 [32] Ph. Rivière, A. Soufiani, Updated band model parameters for H₂O, CO₂,
594 CH₄ and CO radiation at high temperature, *International Journal of*
595 *Heat and Mass Transfer* 55 (2012) 3349–3358.
- 596 [33] C. Ludwig, W. Malkmus, J. Reardon, J. Thomson, *Handbook of in-*
597 *frared radiation from combustion gases*, Technical Report NASA SP-
598 3080, 1973.
- 599 [34] A. Kosareva, O. Kunova, E. Kustova, E. Nagnibeda, Four-temperature
600 kinetic model for CO₂ vibrational relaxation, *Physics of Fluids* 33 (1)
601 (2021) 016103.
- 602 [35] S. J. Young, Band model formulation for inhomogeneous optical paths,
603 *Journal of Quantitative Spectroscopy and Radiative Transfer* 15 (1975)
604 483–501.

- 605 [36] S. J. Young, Nonisothermal band model theory, *Journal of Quantitative*
606 *Spectroscopy and Radiative Transfer* 18 (1977) 1–28.
- 607 [37] S. J. Young, Addendum to: Band model formulation for inhomoge-
608 neous optical paths, *Journal of Quantitative Spectroscopy and Radiative*
609 *Transfer* 15 (1975) 1137–1140.
- 610 [38] P. W. Erdman, E. Zipf, P. Espy, C. Howlett, D. A. Levin, G. V. Candler,
611 In-situ measurements of UV and VUV radiation from a rocket plume
612 and re-entry bow shock, *AIAA Paper* (1992) 92–0124.